



## Experiment NINA: investigation of low energy nuclear fluxes in the near-Earth space

A. Bakaldin<sup>a</sup>, G. Barbiellini<sup>b</sup>, S. Bartalucci<sup>c</sup>, A. Batishev<sup>a</sup>, R. Bellotti<sup>d</sup>, V. Bidoli<sup>e</sup>, M. Boezio<sup>b</sup>, W. Bonvicini<sup>b</sup>, F. Cafagna<sup>d</sup>, M. Casolino<sup>e</sup>, M. Castellano<sup>d</sup>, M. Circella<sup>d</sup>, C. De Marzo<sup>d</sup>, M.P. De Pascale<sup>e</sup>, A.M. Galper<sup>a</sup>, S. Giuntoli<sup>c</sup>, S. Koldashov<sup>a</sup>, M. Korotkov<sup>a</sup>, V. Mikhailov<sup>a</sup>, A. Morselli<sup>e</sup>, A. Murashov<sup>a</sup>, P. Papini<sup>f</sup>, S. Piccardi<sup>f</sup>, P. Picozza<sup>e</sup>, M. Ricci<sup>c</sup>, R. Sparvoli<sup>e,\*</sup>, P. Spillantini<sup>f</sup>, P. Spinelli<sup>d</sup>, A. Vacchi<sup>b</sup>, S. Voronov<sup>a</sup>, N. Zampa<sup>b</sup>

<sup>a</sup> *Moscow Engineering Physics Institute, Moscow, Russian Federation*

<sup>b</sup> *Dept. of Physics, Univ. of Trieste and INFN, Trieste, Italy*

<sup>c</sup> *INFN Laboratori Nazionali di Frascati, Frascati, Italy*

<sup>d</sup> *Dept. of Physics, Univ. of Bari and INFN, Bari, Italy*

<sup>e</sup> *Dept. of Physics, Univ. of Rome "Tor Vergata" and INFN, Roma, Italy*

<sup>f</sup> *Dept. of Physics, Univ. of Firenze and INFN, Firenze, Italy*

Received 4 June 1997; revised 10 October 1997

### Abstract

The mission NINA is the first step of a wide scientific program named WiZard-RIM, conceived to make extensive studies on the Anomalous Component and the isotopic composition of the cosmic rays from hydrogen to iron, in the energy range 10–100 MeV/n. NINA is a silicon detector which is going to fly on the Russian Resource 01 n.4 satellite by the end of 1997. © 1997 Elsevier Science B.V.

PACS: 90.; 95.; 96.; 98.

Keywords: Cosmic rays; Isotopic composition; Satellite; Silicon detector

### 1. Introduction

In the frame of primary cosmic ray investigations, the Italian National Institute of Nuclear Physics (INFN) and the Moscow Engineering Physics Institute (MEPhI) are developing a program of observations with satellite-borne detectors. In particular,

the objectives of the astroparticle physics program WiZard-RIM (Russian–Italian Mission) are the determination of the charge and isotopic composition of the cosmic rays (NINA experiment), the investigation of the cosmic antiparticle fluxes, especially antiprotons and positrons of galactic and extragalactic nature (PAMELA), and the study of the high energy gamma rays from space (GILDA).

The first step of the RIM program is the development of the small-size silicon telescope NINA (RIM-

\* Corresponding author: R. Sparvoli, Dept. of Physics, Univ. of Rome "Tor Vergata" and INFN, Via della Ricerca Scientifica 1, 00133 Rome, Italy. E-mail: Sparvoli@roma2.infn.it.

1), whose goal is to detect cosmic ray nuclei, from hydrogen to iron, between 10 and 100 MeV/n. The experiment will be carried out on board of the satellite Resource-01 n.4; this spacecraft has been developed by the Russian Space Company VNIEM and will be launched on a polar orbit at the end of 1997, during a minimum of solar activity. The mission is intended to last for more than three years.

The technology adopted for the entire mission derives from the development of the silicon calorimeter envisaged for the WiZard experiment on the Astromag facility, which was scheduled to fly on board of the finally canceled Freedom Space Station. It is now used in various WiZard balloon flights with the New Mexico Balloon Facility [1–3].

## 2. Scientific program

One of the most attractive problems still open in astrophysics is the determination of the isotopic composition of the Anomalous Cosmic Rays (ACR's), of the Solar Cosmic Rays (SCR's) and of the Galactic Cosmic Rays (GCR's), as well as of their energetic, temporal and spatial distributions.

### *Anomalous component of cosmic rays*

ACR's were discovered at the beginning of 1970 observing energetic spectra of GCR nuclei in a period of minimal solar activity [4]. It was realized that for energies lower than 50 MeV/n, the abundance of several nuclei (He, O, N, Ne) differed essentially from the expected ones, considering GCR, SCR and solar atmosphere compositions. Typical energetic spectra of ACR and GCR oxygen nuclei during a minimum of solar activity are shown in Fig. 1.

ACR's are nowadays identified as singly-charged interplanetary nuclei (H, He, C, O, Ne and Ar) with energies up to several tens of MeV. They originate from interstellar neutral particles swept into the heliosphere, ionized by solar UV rays or charge exchange with the solar wind, drifted to the outer heliosphere and finally accelerated at its boundary [5]; it is assumed that the ACR acceleration region is located at the solar wind termination shock [6]. The important prediction of this model is that ACR's are mainly singly-ionized. In particular, Klecker et al. [7] recently found that less than 10% of ACR's have a charge greater than 2.

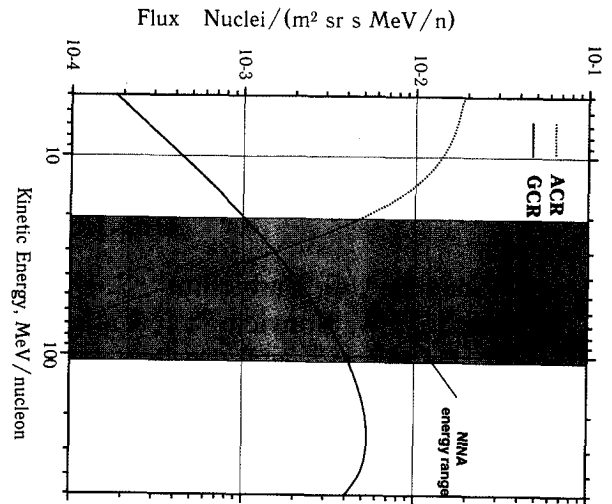


Fig. 1. ACR and GCR interplanetary fluxes for oxygen, in a period of minimum solar activity, together with NINA energetic window in case of TRG1 (see Section 3.3).

Intensity fluctuations of ACR's, resulting from a solar wind modulation during the solar cycle, bring to variations of the spectrum index, in the energy range 10–50 MeV/n, from +1 (absence of ACR's) to –1 (maximum of ACR intensity). This behavior, which is in agreement with GCR solar modulations, together with the observed ACR intensity gradient in the interplanetary space [8] (ACR flux higher at longer distances from the Sun), can confirm the hypothesis that ACR's penetrate into the heliosphere from outside (heliosphere boundary or interstellar medium).

A very important step towards the comprehension of the ACR phenomenon was done by experiments on board of the satellite COSMOS (altitude 200–280 km), realized as well during a minimum of solar activity [9,10]. In this experiment the Earth's magnetic field was used as a spectrometer for cosmic ray energetic ions to determine their degree of ionization. ACR nuclei were discovered in the near-Earth space: these fluxes were surely anomalous, because fully "stripped" nuclei with energies about 10–50 MeV/n could have not penetrated inside the Earth's magnetosphere (L-shell  $\sim 2$ ) due to the geomagnetic cutoff effect. The discovery of trapped ACR's was, therefore, a further confirmation of unitary charged

anomalous nuclei outside the magnetosphere.

Following these observations it was shown [11,12] that ACR nuclei trapped by the Earth's geomagnetic field form radiation belts. As a consequence, the following process for ACR accumulation in the geomagnetic trap was proposed: first, single-ionized anomalous ions penetrate into a low value L-shell, due to their small charge, and are stripped by the high altitude residual atmosphere; afterwards nuclei get trapped by the geomagnetic field and oscillate for a long time. The lifetime of this belt is determined by ionization loss processes [13].

Blake et al. in 1991 [14] proposed a geomagnetic distribution model of trapped anomalous oxygen nuclei, while Tylka in 1993 [15] presented the geographic distribution map of these nuclei at low altitudes, from several hundreds up to thousand kilometers.

Since their discovery, ACR's have been extensively studied by means of numerous missions.

With experiments on board of COSMOS satellites (1966–1988, altitude 200–400 km, inclination 70.4–82.3°), studies of oxygen nuclei fluxes in the energy range 4–25 MeV/n were carried out and ACR's were discovered in the magnetosphere [11,16]. The mission AHURADHA (1985, altitude 352 km, inclination 57°) studied ACR as well as iron nuclei fluxes between 10 and 150 MeV/n [17]. In experiments on board of LDEF satellites (1984–1990, altitude 476, inclination 28.53°), investigations of nuclei with charge greater than 6 and energies more than 15 MeV/n were performed [18]. Finally, the COSMOS 2260 experiment (1993, altitude 280 km, inclination 82.3°) investigated fluxes of oxygen nuclei in the energy range 20–40 MeV/n [19].

It should be noted that the experiments mentioned above made use of passive plastic nuclear track detectors, which give information about the pitch-angle and geographic coordinates of the observed particles.

Starting from July 1992, a year of maximum solar activity, and still in progress, a full-scale study of the nuclear component of cosmic rays from H up to Ni, in an energy range from several MeV/n up to several hundreds, has been carried out by the SAMPEX satellite using four different instruments (LEICA, HILT, MAST, PET) [20]. This is the only experiment, so far, interested in ACR's that uses active detectors (semiconductors, scintillators), which pro-

vide complete particle information.

Despite the large number of experiments dealing with ACR's, a detailed study of their physical processes is still limited by the absence of a complete and statistically reliable set of experimental data, in different periods of the solar activity cycle.

An important improvement in the comprehension of ACR's could arrive from a detailed investigation of the spatial, pitch-angle, energetic and temporal distributions of He, O, N, Ne and other nuclei in the near-Earth space, including the regions of geomagnetic capture, during the complete new 23rd cycle of solar activity, starting from its minimum (1996). At present, several experiments dealing with the study of ACR's are under development; the program NINA occupies an important place among the proposed projects.

#### *Solar cosmic rays*

Despite the great number of experiments (SAMPEX [20], CRRES [21]), already carried out or still in progress, dedicated to the study of charge and isotopic compositions of solar flare fluxes, the problem of nuclear production, propagation in the interplanetary space and penetration into the Earth's magnetosphere in presence of strong solar flares is still not clear.

The high energy component of solar particles is formed during flares. In most cases, charge and isotopic flare compositions are continuous and correspond to those of the solar atmosphere, but under particular conditions they can instead strongly depend on the intensity and type of flare and therefore can change from flare to flare as well as during a single event. As an example, the ratio between proton and helium fluxes for energies greater than 20 MeV/n can vary from 1 till 300 [22].

Another peculiarity of some solar flares is the enrichment of heavy elements (iron group) in relation to the composition of the solar atmosphere, as well as a changing in the  $^3\text{He}/^4\text{He}$  ratio from  $10^{-2}$  up to 1–8 [23]. The origin of these phenomena has not been clarified so far. Finally, it is important to study the isotopic ratios of the hydrogen group (H, D, T) coming from solar flares.

In order to clarify the physical processes related to flares, it is necessary to carry out more detailed investigations of the charge and isotopic composition of SCR's; the experiment NINA will give the possibility

to study the charge and isotopic composition of SCR's in the polar sectors of the orbit with a high quality mass resolution.

### *Galactic cosmic rays*

A detailed study of the nuclear and isotopic composition of GCR's as well as of their dynamics is always of great interest in astrophysics, due to the variations of GCR's fluxes with the solar activity. GCR's are nuclei with energies exceeding several MeV/n as well as electrons and positrons with energies greater than 10 MeV. Sources of such particles, coming into the interplanetary space from the interstellar medium, are supernovae and new stars of the galaxy. It is also possible that particles with energy lower than few hundreds of MeV/n are accelerated in the interplanetary medium by the solar wind in the wind termination shock region.

Long-term and continuous observations of GCR and SCR fluxes will allow us to find out which effects, in the temporal and energetic particle flux parameters, are definitely connected to the heliosphere modulation induced by the solar activity.

## 3. The instrument NINA

The telescope NINA will fly on board of the Russian VNIEM satellite Resource-01, version n.4. It consists of four parts: the *detector D1*, the *on board processors* for data handling *D2*, the *computer interface* with the satellite *E* and finally the *power supply P*. The weight and electric power allowed for all the telescope parts are respectively 40 kg and 40 W.

Following the usual flight mission procedures, NINA has already been built in two versions: a so-called *engineering model*, used for all functionality tests and compatibility operations with the satellite, and a *flight model*, equal to the previous one, which will be finally installed on the spacecraft and fly.

### 3.1. The silicon detector

The active part D1 of NINA instrument is formed by a telescope made of 16 silicon planes. Each sensitive element consists of two n-type silicon detectors,  $60 \times 60 \text{ mm}^2$ , attached to a supporting ceramic frame. The 16 strips of the two views are orthogonal in order



Fig. 2. Photograph of NINA detector.

to measure  $x, y$  coordinates of the detected particle. The thickness of the first two detectors is  $150 \mu\text{m}$ , in order to explore lower energies; all the others, instead, are  $380 \mu\text{m}$  thick, so to have 11.7 silicon mm in total.

A photograph of the detector is shown in Fig. 2. The 16 Si detector planes are vertically stacked; the interplanar distance is 1.4 cm; only the first and second planes are separated by 8.5 cm, for a better measurement of the particle incident angle, resulting in a total telescope height of 29.5 cm. An aluminum cover of just  $300 \mu\text{m}$  is placed on top of the detector.

NINA's geometrical factor is  $8.3 \text{ cm}^2\text{sr}$  for low energy particles which stop in the second plane, and it decreases with growing energy. Fig. 3 shows the be-

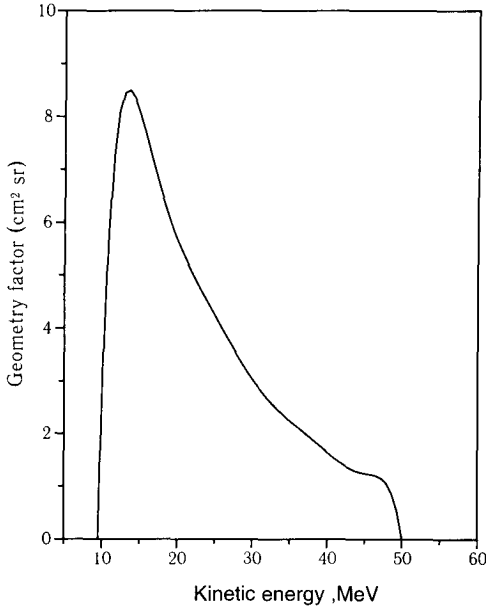


Fig. 3. Geometric factor of NINA detector as a function of energy, calculated for protons entering the detector, with TRG1 selected (see Section 3.3).

havior of Nina's GF for protons, in case of TRG1 (Section 3.3).

### 3.2. Front-end electronics

The signal produced by the charge released by the incoming particles has to be shaped before performing conversion. The front-end electronic system is the evolution of the one we are using on balloon flights. Every layer of the telescope has two 16 channels preamplifiers. The analysis chain of a single strip signal is shown in Fig. 4.

The signal of each strip is shaped by a unipolar  $CR - RC * RC$  filter used in input to the ADC, while the bipolar  $CR * CR - RC$  system governs the Zero Crossing Discriminator used in the trigger logic. A multiplexer system addresses each strip of the detector for digital conversion by the working ADC and sends the converted data to the FIFO to D2. With a clock speed of 250 kHz, the 512 ( $16 \times 16 \times 2$ ) required conversions are performed in about 2 ms.

The dynamic range of the system is of a factor 1000, allowing the detection of a single strip energy deposition up to 280 MeV.

### 3.3. Trigger logic

In the telemetry sharing among the different experiments on board of the satellite, the trigger logic has to ensure a highly efficient event acquisition, rejecting particles not stopping inside the calorimeter.

The veto system ensuring the containment is performed setting in anticoincidence the strips 1 and 16 of planes from 2 up to 15, and all plane 16 strips.

The basic operating trigger of the acquisition system is the following:

$$\text{TRG1} = A_{1x} \times A_{1y} \times ((A_{2x} + A_{2y}) + (A_{3x} + A_{3y})) \times \overline{A_{16x}} \times \overline{A_{16y}} \times \overline{\text{LAT}}, \quad (1)$$

where  $A_{ij}$  is the signal coming from strips 2 to 15 of plane  $i$  ( $i = 1, 16$ ), view  $j$  ( $j = x, y$ ) and LAT is the logic OR of all signals coming from the strips defining the lateral anticoincidence. The logic OR of planes 2 and 3 provides redundancy in case of a failure of plane 2. In the trigger it is also assumed that the signal released by the particle in both views of the first plane must be under the saturation limit of the ADC (280 MeV).

In particular data taking configurations, or in case of failure of the first plane, it is possible to switch, via a telecommand, to a second trigger logic:

$$\text{TRG2} = (A_{2x} + A_{2y}) \times (A_{3x} + A_{3y}) \times (A_{4x} + A_{4y}) \times \overline{A_{16x}} \times \overline{A_{16y}} \times \overline{\text{LAT}}. \quad (2)$$

In case of hardware malfunctioning of the lateral anticoincidences, they can be removed from the trigger via a dedicated ground command. Finally, to study particles crossing the whole telescope it is possible to exclude, again via telecommand, the bottom veto.

The default threshold for the trigger is set to 250 KeV in order to eliminate all relativistic particles (Low Threshold). A second threshold, fixed at 1200 KeV for the first two thin detectors and at 2500 KeV for the others, has been foreseen in order to select the detection of  $Z > 1$  nuclei (High Threshold).

### 3.4. Acquisition modes

The 512 event matrix from the telescope is read by the on-board microprocessor; this performs gain

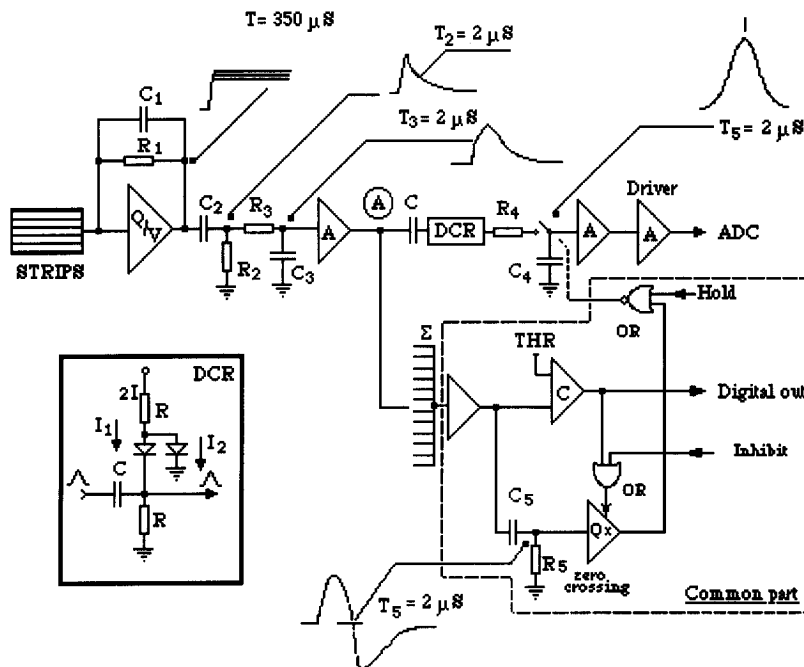


Fig. 4. Electric scheme of a single electronic channel.

calibration, pedestal subtraction and zero suppression for each channel.

The particle rate changes very fast along the orbit so that the operation mode has to be adapted to the local particle flux conditions. In automatic operation, 3 data acquisition and storage modes are foreseen, depending on the counting rate:

- (1) **Low rate** (up to 10 Hz). This *full-format mode*, in which the whole event topology is recorded, is the normal working configuration outside the Earth Radiation Belts. It allows us to measure the energy released by the particle in each detector (Bragg curve). Within the precision allowed by the strip pitch, we can also reconstruct the particle trajectory, identify its range with good precision, check for multiple tracks and for particles escaping the telescope due to the geometrical inefficiency of the anticoincidence system.
- (2) **High rate** (10–100 Hz). At high fluxes, to make an optimal use of the mass memory storage, the second microprocessor calculates the total energy released in the first plane ( $E_1$ ) and in the whole detector ( $E_{tot}$ ) by the crossing particle. To select mainly single and non-escaping tracks,

a “second level trigger” restricts the event acceptance to particles crossing the 4 central strips of the first 3 planes of the telescope, leaving a single cluster (multiple tracks subtraction) of fired strips. Once these conditions have been fulfilled, only the  $E_1$  and  $E_{tot}$  information of the event is transmitted ( $E_1$ – $E_{tot}$  mode).

- (3) **Rate meter** (above 100 Hz). If the trigger rate rises above 100 Hz, only the counting rates of certain planes, chosen at different depths of the telescope, are stored (*rate-meter mode*). In this configuration, the logic signal from the plane is sent to an integrating RC system, whose value is read and stored every 6 minutes.

### 3.5. Telecommands

The interaction between the Ground Station and NINA during the flight is driven by 22 telecommands. Some are dedicated to operations like power switching ON/OFF, data transferring, memory cleaning, single or dual microprocessor mode setting. The others act on the trigger logic or on the storage model, having therefore a direct effect on the data collection.

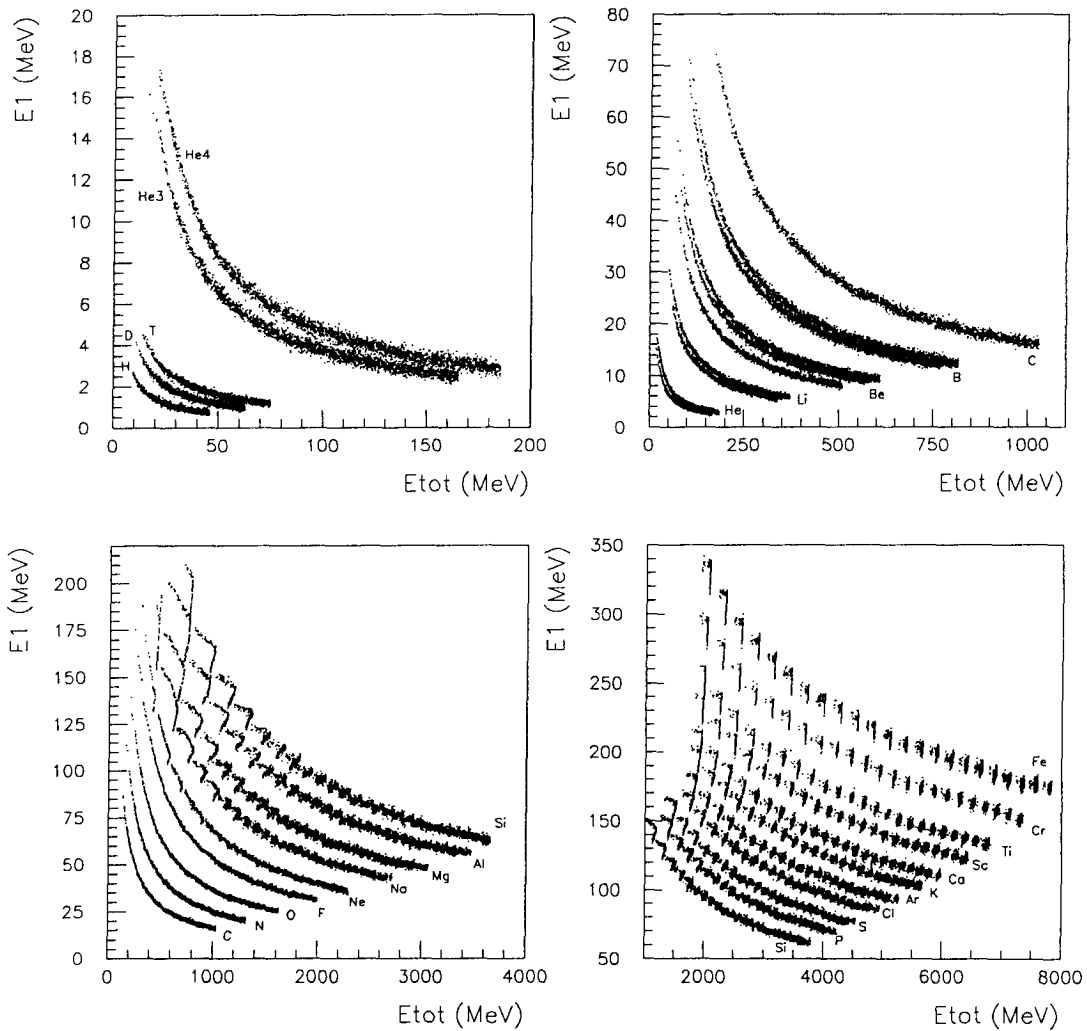


Fig. 5. Energy released in the first plane ( $E_1$ ) vs energy released in the whole detector ( $E_{tot}$ ) for several nuclei in NINA (MC simulations); energies are expressed in MeV. Upper left: H, D, T,  $^3\text{He}$ ,  $^4\text{He}$ ; upper right: He, Li, Be, B, C; bottom left: C, N, O, F, Ne, Na, Mg, Al, Si; bottom right: Si, P, S, Cl, Ar, K, Ca, Sc, Ti, Cr, Fe.

The default condition of the telecommand set imposes an event acquisition with the Trigger 1 (TRG1), Low Threshold (L.T.), lateral strips and bottom plane in anticoincidence, and acquisition mode automatically switching to the different options already mentioned depending on the rate conditions. Nevertheless, it is possible by telecommands to exclude this automatic procedure and impose a particular acquisition status: switching, for instance, to the second trigger (TRG2), setting the High Threshold (H.T.), fixing the data storage mode to  $E_1$ - $E_{tot}$  or *full-format mode*,

turning OFF the lateral anticoincidence strips, switching OFF the bottom anticoincidence strips or, in case of malfunctioning of plane 16, using plane 15 as a bottom veto system.

### 3.6. On-board processors D2

After conversion by ADCs, data are sent through a FIFO to an 8 channel bus interface with D2. Here all tasks of event processing are performed before sending the data to  $E$  for mass memory storage.

Table 1  
Energy windows for the most abundant particles in NINA detector

Particle	Z	A	$E_{\min}$ (MeV/n)	$E_{\max}$ (MeV/n)	$E_{\min} - \text{TRG2}$ (MeV/n)
H	1	1	10.0	48.0	18
D	1	2	6.5	32.0	12.5
T	1	3	5.0	25.3	9.7
$^3\text{He}$	2	3	11.0	55.7	21.3
$^4\text{He}$	2	4	9.25	47.2	18.0
$^6\text{Li}$	3	6	11.5	59.3	22.7
$^7\text{Li}$	3	7	10.6	54.4	20.7
$^7\text{Be}$	4	7	14.6	75.1	28.6
$^9\text{Be}$	4	9	12.7	65.2	24.8
$^{10}\text{B}$	5	10	16.0	79.0	31.0
$^{11}\text{B}$	5	11	14.6	74.6	29.1
C	6	12	17.5	87.5	33.3
N	7	14	18.6	95.0	36.4
O	8	16	20.0	103.1	39.4
F	9	19	21.0	106.8	40.5
Ne	10	20	23.0	117.0	44.5
Si	14	28	27.5	141.8	53.6
Ca	20	40	38.5	174.5	65.3
Fe	26	56	58.2	194.6	72.5

Column 3:  $E_{\min}$  using TRG1. Column 5:  $E_{\min}$  using TRG2.

The core of *D2* are two 8086 microprocessors working with a clock speed of 4 Mhz. The first microprocessor receives the event data from *D1* and performs pedestal suppression and data reduction tasks, while the second is used to format the data, according to the acquisition mode, and send them to *E*. It also selects the trigger logic, implements the second level trigger and interfaces most of the telecommands with *D1*.

This redundant architecture allows the system to work with a maximum acquisition speed of 100 Hz. In case of failure of one of the two 8086, all tasks can be performed – at a reduced speed – by the remaining one.

#### 4. NINA performances

NINA energy windows for the most abundant chemical elements are reported in Table 1.

##### 4.1. Simulation results

The detector performances have been studied with computer simulations using the Geant 3.21 Monte Carlo program.

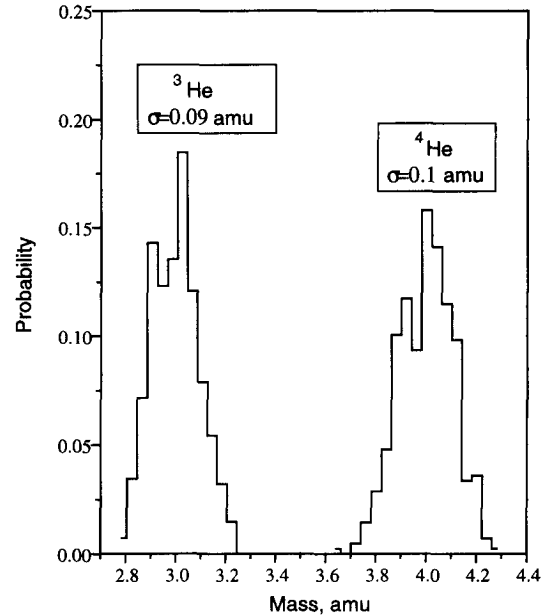


Fig. 6.  $^3\text{He}/^4\text{He}$  discrimination obtained with the Bragg curve minimization algorithm (MC data). The probability is shown on the y-axis.

A fast and straightforward nuclear and isotope discrimination can be performed with the  $dE/dx$  vs  $E$  technique. The simulated response for several nuclei from H to Fe in the acceptance window of the calorimeter is shown in Fig. 5, where the energy released in the first plane of the detector versus the total deposited energy is plotted. Energies are expressed in MeV. It is evident that, with this technique, nuclear discrimination is successfully performed for all  $Z$  particles and even light nuclei isotope discrimination is possible.

For heavy particles, starting from Ne, the ADC saturation, due to a released energy exceeding 280 MeV, starts to occur at the end of the particle Bragg curve; other algorithms that make use of the information coming from all Si detectors, to improve NINA recognition, must therefore be developed in this case.

A significant improvement of the NINA nuclear and isotopic resolution can be obtained by algorithms using all the Bragg curve obtained by means of the energy released in the crossed layers. Results for  $^3\text{He}/^4\text{He}$  discrimination obtained with this method are shown in Fig. 6, for helium stopping at plane 8 of the detector (MC data).

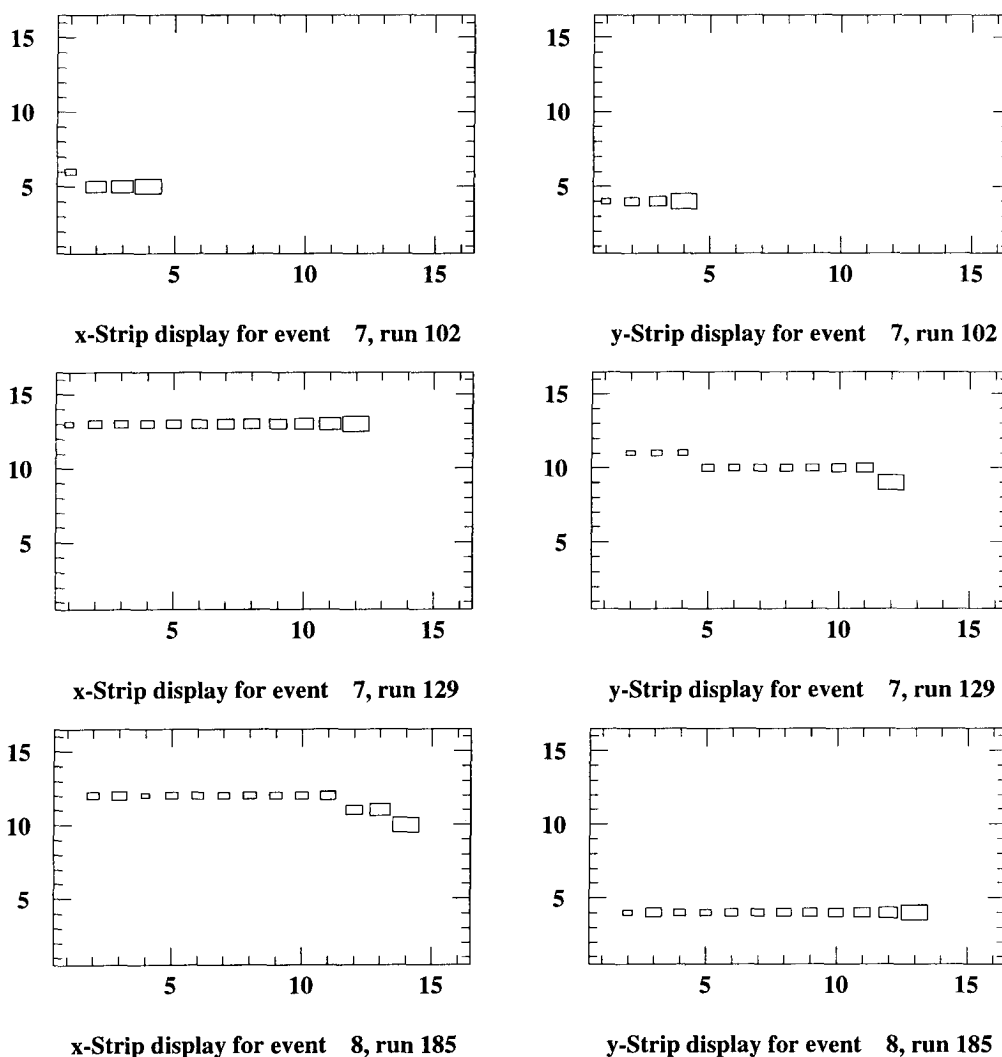


Fig. 7. Tracks inside NINA detector from the beam test at PSI (March 1996). Upper two: 120 MeV  $\alpha$  ( $x$  and  $y$  view); central two: 60 MeV D ( $x$  and  $y$  view); bottom two: 50 MeV P ( $x$  and  $y$  view). For each graph, the  $x$ -axis represents the plane number ( $1 < p < 16$ ), and the  $y$ -axis the strip number ( $1 < s < 16$ ).

The best mass reconstruction, anyway, can be achieved in NINA by using the Range-Energy technique, as shown in Fig. 10.

#### 4.2. Accelerator tests

Beam tests of NINA *engineering model* have been performed at the Cyclotron of the PSI Laboratory at Villigen (Zurich), while the *flight model* has been calibrated at the SIS Synchrotron of the GSI Laboratory

at Darmstadt.

At PSI, 120 MeV alphas, 60 MeV deuterons, 50 and 71 MeV protons have been used to test the telescope performances and measure the trigger and the anticoincidence efficiencies. Some particle patterns in NINA and their corresponding Bragg curves are shown in Figs. 7 and 8.

At GSI, the flight model has been tested in its final space configuration, using therefore all the devices finally installed on the Resource satellite. A Ground

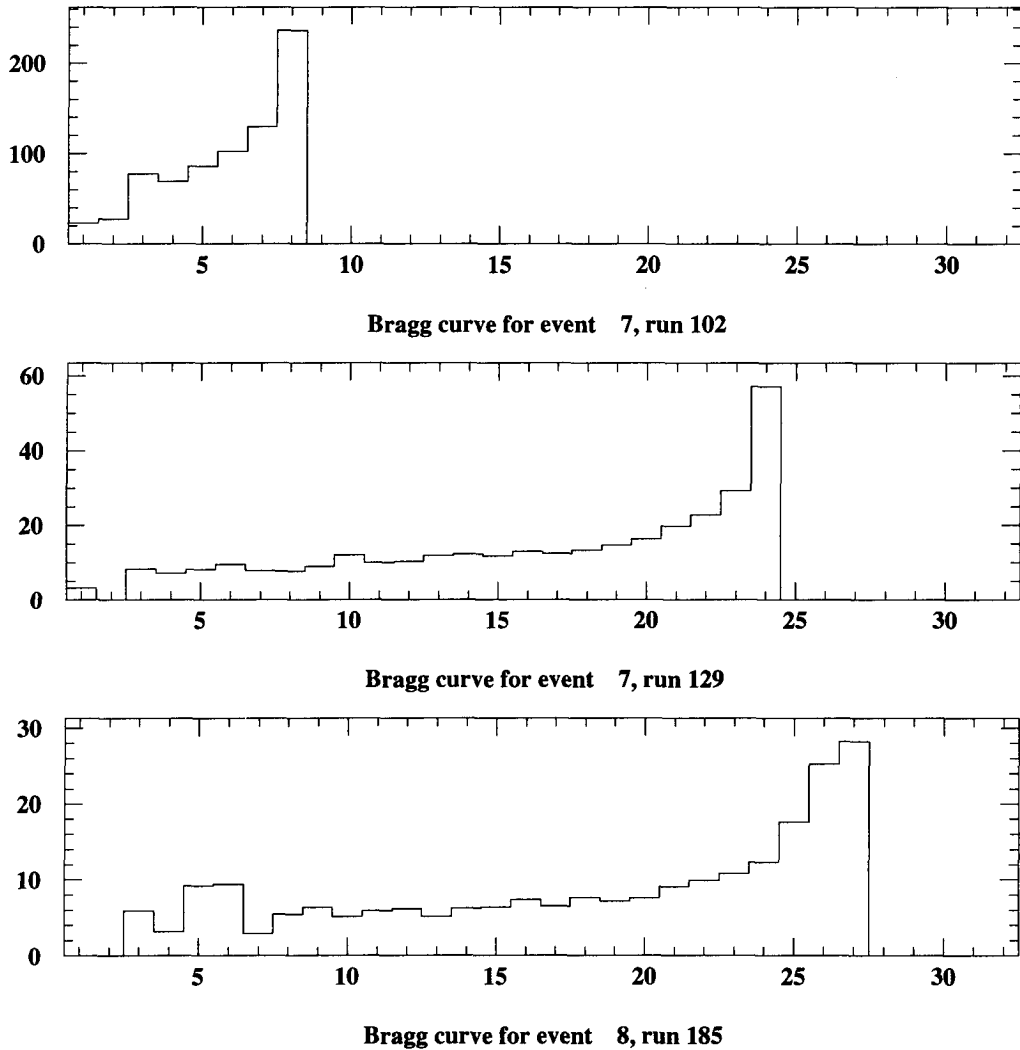


Fig. 8. Bragg curves of tracks inside NINA detector from the beam test at PSI (March 1996). Upper: 120 MeV  $\alpha$ ; Central: 60 MeV D; Bottom: 50 MeV P. For each graph, the  $x$ -axis represents the view number ( $1 < v < 32$ ), and the  $y$ -axis the corresponding energy contents, expressed in ADC channels.

Segmented Equipment (GSE) was built and used during the tests to simulate all the satellite central computer operations, like receiving telecommands from Ground and transmitting them to the apparatus, transferring data from  $E$  to the common spacecraft memory and then, via telemetry, to Earth.

A  $^{12}\text{C}$  beam at energies of 65, 80, 100 and 300 MeV/n was available for the test. Data have been taken in different conditions. Direct  $^{12}\text{C}$  beam runs have been used for energy calibration; others, by in-

terposing a polyethylene target between the detector and the beam, to favour fragmentation products and so test the NINA discrimination capability, have also been performed.

Some significant results obtained with GSI data are reported in Figs. 9 and 10. In Fig. 9 it is shown that the  $E_1$  vs  $E_{\text{tot}}$  technique is quite an effective means to determine the nuclear charge of the particles; energies are expressed in ADC channels, each channel corresponding to 74 keV. In Fig. 10, instead, a good mass

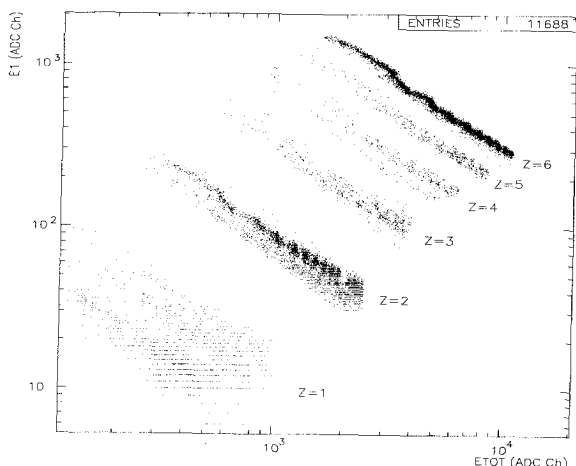


Fig. 9.  $E_1$  vs  $E_{tot}$  for real data at GSI (April–May 1997); energies are in ADC channels. Products from  $^{12}\text{C}$  ( $Z = 6$ ) fragmentation are visible.

reconstruction (MeV) by the Range-Energy technique for  $Z = 1$  and  $Z = 2$  nuclei is presented. Nuclei in both graphs derive from fragmentation of a  $^{12}\text{C}$  beam at 300 MeV/n.

## 5. Orbit conditions and expected rates

The Resource-01 n.4 satellite will be sent on a polar orbit, with altitude 835 km, inclination  $98^\circ$  and axis pointed to the zenith. It will have a period of 6100 seconds so to make about 14 revolutions per day. The orbit parameters allow us to carry out measurements in different conditions: around the poles, where no particles are trapped by the Earth's magnetosphere, it will be possible to study fluxes of GCR and SCR nuclei as well as of nontrapped ACR's; inside the Earth's magnetosphere at medium latitudes, where no low energy GCR nuclei are present due to the geomagnetic cut-off effect, the instrument will give us the possibility to fulfill the observation of ACR fluxes without contamination by GCR's; finally, on the remaining part of the orbit, when the satellite will be situated inside the Earth Inner Radiation Belt, studies of fluxes of trapped ACR nuclei will be carried out.

The quality of the measurements will be determined by the background conditions, which change widely along the satellite trajectory as for the particle species and the flux intensities. In the high latitude region, in fact, low energy electrons belonging to the Outer

Radiation Belt are the main contribution to the background flux. In the region inside the Inner Radiation Belt, instead, protons act like that.

In order to estimate the background conditions on the orbit as well as the number of collected events by NINA during its lifetime, models of proton and electron fluxes in the near-Earth space have been used [24]. Real parameters of the orbit for the evaluation of the satellite trajectories and the determination of the geographical coordinates have been considered; the instrument axis orientation towards the zenith has been taken into account as well. Finally, knowing the instrument characteristics (geometrical factor, temporal, energetic and angular parameters), the expected counting rates of the detector in different conditions have been estimated.

The counting rate of the instrument versus time with TRG1 and Low Threshold for a whole orbit, with hard background conditions, is shown in Fig. 11; as one can see, the counting rate changes from  $10^{-1}$  Hz up to  $10^4$  Hz. Regions of *full-format mode* operations are shaded with lines. Even for very hard background conditions, the observation time is not less than 50% of the satellite revolution time. For better conditions, regions of *full-format mode* would be wider.

Despite the quite low counting rate of the trigger system ( $\leq 2 \times 10^2$  Hz), it is practically impossible to carry out measurements in the Outer Radiation Belt, due to the large number of relativistic electrons reaching the detector, resulting in multiple superposition of signals. On the other hand, observation of particles in the Inner Belt is possible only on its boundaries, where the counting rate of the instrument does not exceed  $10^2$  Hz (see again Fig. 11). These limitations remain during the operation with High Threshold.

In conclusion, NINA instrument will allow the registration of GCR, SCR, ACR nuclei (regions II, IV on Fig. 11) at high latitudes as well as fluxes of ACR and high energy GCR nuclei inside the Earth's magnetosphere outside the Radiation Belts (regions I, III, V) at medium latitudes. Finally, studies of trapped ACR's will be carried out only at the boundaries of the Inner Radiation Belts during short time intervals.

In Table 2 expected numbers of different GCR (from H up to Fe) and ACR nuclei with low and high threshold acquisition conditions during one day are presented.

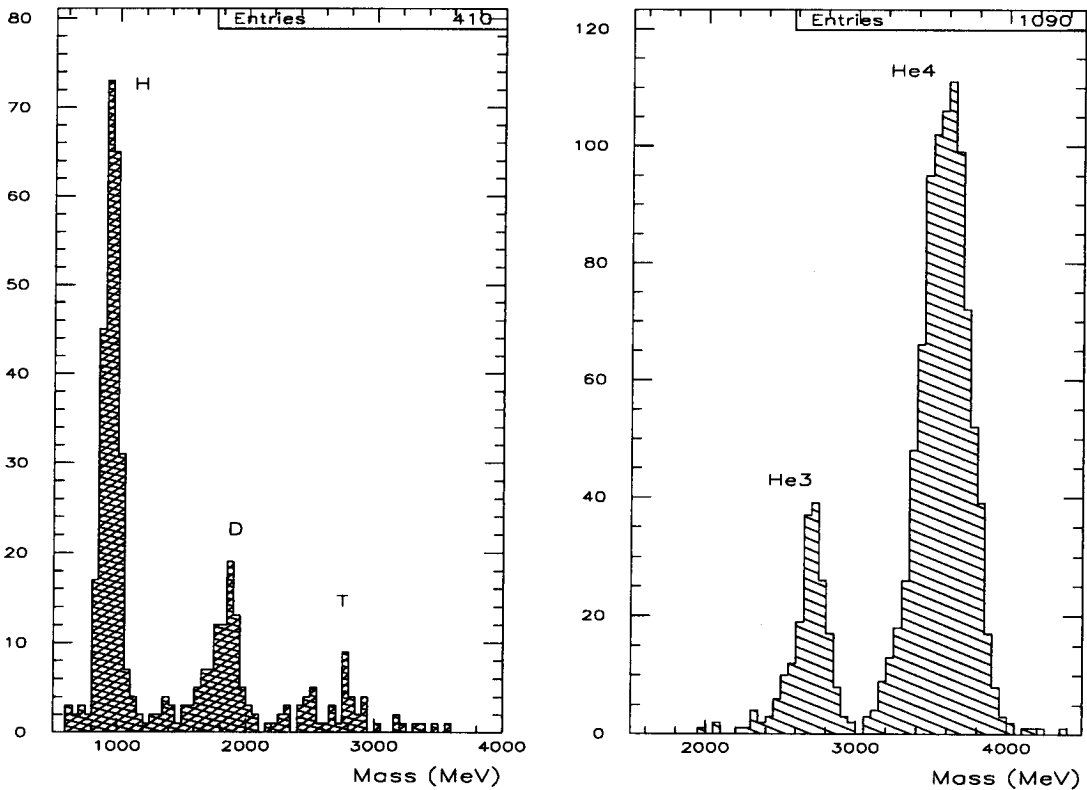


Fig. 10. Mass reconstruction with Range-Energy techniques for real data at GSI (April-May 1997). Masses are in MeV. Left: H, D, T, right:  $^3\text{He}$ ,  $^4\text{He}$ . The number of events are shown on the y-axis.

Table 2

Expected number of nuclei/day for NINA detector (period of minimum solar activity)

	H	He	Li	Be	B	C	N	O	F	Ne	Na	Ar	Fe
GCR (H.T.); regions II, IV	-	186	2	2	13	29	10	39	2	7	2	2	2
ACR (H.T.); regions II, IV	-	10.5	-	-	-	0.07	0.9	4.2	-	0.05	-	0.05	-
ACR (H.T.); regions I, III, V	-	2.6	-	-	-	0.04	0.5	2.5	-	0.03	-	0.04	-
GCR (L.T.); regions II, IV	136	157	1.5	1.5	10	23	8	30	1.3	6	1.7	1.4	1.7

H.T. and L.T. indicate respectively the High Threshold and Low Threshold regimes; regions I, II, III, IV, V refer to Fig. 11.

## 6. Conclusions

The NINA silicon telescope, developed for deepening our knowledge on the solar and galactic cosmic rays between 10 and 100 MeV/n, has been constructed in two exemplars. The first, the *engineering model*, has been tested at the PSI accelerator and installed on the Resource 01 n.4 satellite for final compatibility tests. The *flight model*, instead, has been calibrated at the

GSI Laboratory and will be integrated on the satellite in July 1997.

The window for the launch from the space base of Baikonour in Kazakhstan is fixed for the period September–November 1997.

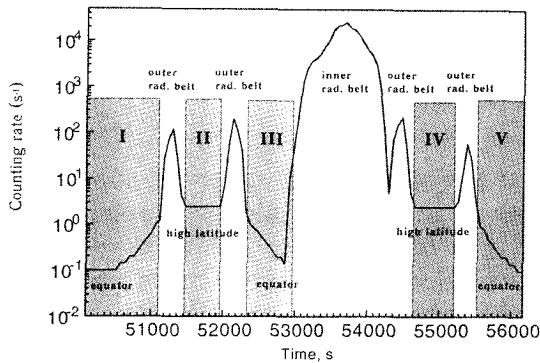


Fig. 11. NINA trigger counting rate along a single orbit.

### Acknowledgements

We acknowledge Laben (Italy) for the realization of *D1* and *D2* parts of the detector, as well as VNI-IEM for parts *E*, *P* and especially for all the operations related to the Resource satellite. We also would like to thank all the staff at PSI (Zurich) and GSI (Darmstadt) Laboratory for their kind cooperation.

Finally we acknowledge the State Committee of Science and Technology of the Russian Federation, who partially supported this work.

### References

- [1] R.L. Golden et al., *Il Nuovo Cimento* 105 B (1990) 191.
- [2] F. Aversa et al., *NIM A* 360 (1995) 17.
- [3] M. Bocciolini et al., *NIM A* 370 (1996) 403.

- [4] W.R. Webber et al., *Proc. 14th Int. Cosmic Ray Conference*, Vol. 5, Munich (1975) p. 1597.
- [5] L.A. Fisk, B. Kozlovsky, R. Ramaty, *Astrophys. J.* 190 (1974) L39.
- [6] M.E. Pesses, J.R. Jokipii et al., *Astrophys. J.* 246 (1981) L85.
- [7] B. Klecker et al., *Proc. 24th Int. Cosmic Ray Conference*, Vol. 4, Rome (1995) p. 489.
- [8] J.H. Adams et al., *Astrophys. J.* 377 (1991) 292.
- [9] A. Dutta, J.N. Goswami, *Proc. 22nd Int. Cosmic Ray Conference*, Vol. 3, Dublin (1991) p. 346.
- [10] J.H. Adams et al., *Proc. 22nd Int. Cosmic Ray Conference*, Vol. 3, Dublin (1991) p. 358.
- [11] V.V. Bobrovskaya, N.L. Grigorov et al., *Proc. 23rd Int. Cosmic Ray Conference*, Vol. 3, Calgary (1993) p. 432.
- [12] J.R. Cummings et al., *Proc. 23rd Int. Cosmic Ray Conference*, Vol. 3, Calgary (1993) p. 428.
- [13] V.D. Ilin et al., *Space Research*, Vol. N (1993) p. 115.
- [14] J.B. Blake, M. Schulz, M.C. McNab, *Proc. 22nd Int. Cosmic Ray Conference*, Vol. 3, Dublin (1991) p. 629.
- [15] A.J. Tylka et al., *Proc. 23th Int. Cosmic Ray Conference*, Vol. 3, Calgary (1993) p. 436.
- [16] A.J. Tylka et al., *Proc. 24th Int. Cosmic Ray Conference*, Vol. 4, Rome (1995) p. 485.
- [17] J.S. Yadav et al., *Proc. 24th Int. Cosmic Ray Conference*, Vol. 4, Rome (1995) p. 493.
- [18] T. Kleis et al., *Proc. 24th Int. Cosmic Ray Conference*, Vol. 4, Rome (1995) p. 481.
- [19] M. Leicher et al., *Proc. 24th Int. Cosmic Ray Conference*, Vol. 4, Rome (1995) p. 1017.
- [20] D.N. Baker et al., *IEEE Transactions on geoscience, Remote Sensing* 31 (1993) 531.
- [21] J.B. Blake, *STEP* 2 (1992) 1.
- [22] R.P. Lin et al., *Astrophys. J.* 253 (1982) 949.
- [23] S.A. Colgate et al., *Astrophys. J.* 213 (1977) 849.
- [24] S.V. Avakyan et al., *Gidrometioisdat* (1994).